# Synthesis of Dual Z-Scheme CuBi$_2$O$_4$/Bi$_2$Sn$_2$O$_7$/Sn$_3$O$_4$ Photocatalysts with Enhanced Photocatalytic Performance for the Degradation of Tetracycline under Visible Light Irradiation

Jingjing Xu *, Yanlin Zhu, Zeyu Liu, Xueyu Teng, Haiqing Gao, Yaxin Zhao and Mindong Chen

Jiangsu Key Laboratory of Atmospheric Environment Monitoring and Pollution Control, School of Environmental Science and Engineering, Collaborative Innovation Center of Atmospheric Environment and Equipment Technology, Jiangsu Engineering Technology Research Center of Environmental Cleaning Materials, Nanjing University of Information Science and Technology, Nanjing 210044, China; zhuyanlin1998@163.com (Y.Z.); liuzeyu7404@163.com (Z.L.); tengxueyunuist@163.com (X.T.); haiqinggaonuist@163.com (H.G.); yaxinzhaonuist@163.com (Y.Z.); chenmdnuist@163.com (M.C.)
* Correspondence: xujj@nuist.edu.cn; Tel./Fax: +86-25-58731090

**Abstract:** The dual Z-scheme heterojunction CuBi$_2$O$_4$/Bi$_2$Sn$_2$O$_7$/Sn$_3$O$_4$(CBS) was successfully constructed through in situ growth methods, and its photocatalytic performance was evaluated via degradation of tetracycline hydrochloride under visible light. Out of all samples, CBS-2 exhibited the highest photocatalytic activity, with an apparent rate constant of 2.34, 20.16, and 44.17 times that of Bi$_2$Sn$_2$O$_7$, CuBi$_2$O$_4$, and Sn$_3$O$_4$, respectively. Even after four cycles, the photocatalytic efficiency remained above 85%. The improvement can be attributed to the construction of the Z-scheme heterojunction, which effectively promotes the separation and migration of photogenerated carriers. The possible photocatalytic degradation mechanism of dual Z-scheme heterojunction CBS was deduced based on the theory of free radical capture and energy band.

**Keywords:** dual Z-scheme; photocatalysis; tetracycline; visible light

## 1. Introduction

In recent years, antibiotics have been widely used in many fields, but at the same time, they are difficult for the human body to completely metabolize, and a large quantity of them enter the water environment through the digestive system, causing increasing water pollution. Furthermore, they are reabsorbed by the human body through the water environment, which is harmful to human health [1–4]. Therefore, antibiotic pollution has become a major problem in water pollution control. Among them, tetracycline, as a class of common broad-spectrum antibiotics, is widely used in animal husbandry and animal medicine, but due to years of overuse, its residues exist in the water environment for a long time and are difficult to degrade [5]. Therefore, safe and effective removal methods have received extensive attention.

Commonly used methods for the removal of antibiotics are adsorption [6,7] and biodegradation [8,9], but their shortcomings are also obvious: the enrichment transfer process producing secondary pollution, the low removal efficiency, the high price, the more toxic by-products, and the large energy consumption. Photocatalysis can be used as a safe, effective, and environmentally friendly method to degrade tetracycline [10–13]. Mukhtar et al. prepared dual Z-scheme core–shell PANI-CeO$_2$-Fe$_2$O$_3$-NiO heterojunctions to remove MB and MO dyes, with removal rates of 99% and 98%. Increased photocatalytic activity can be attributed to dual Z-scheme formation and the core–shell morphology of PANl, which effectively promote the separation of photogenerated carriers [14]. Munawar et al. prepared a dual Z-scheme Sm$_2$O$_3$-WO$_3$-La$_2$O$_3$ nanocomposite to remove MB and MO dyes, with removal rates of 99% and 96% [15]. However, its photocatalytic stability, absorption spectrum range, and degradation capability limit its further application.

Therefore, the development of stable, efficient, and visible light photocatalysts is one of the most important objectives in the field of photocatalysis.

$Bi_2Sn_2O_7$(BSO) is a Bi-based pyrochlore structure photocatalyst with the advantages of a moderate band gap (2.7 eV), adjustable structure, low cost, easy doping modification, and non-toxicity [16–20]. However, the high recombination rate of photogenerated electrons and holes and poor quantum efficiency limit the improvement of its photocatalytic performance [21–23]. Among many methods for improving photocatalytic performance, the construction of heterojunction structures is one of the most effective methods [24–26]. The Z-scheme heterojunction couples two semiconductors with matching band gaps, based on maintaining the light absorption range, by which the separation efficiency and redox capacity of carriers are improved, therefore improving the photocatalytic performance [19,23,27]. Considering the relatively positive CB potential of BSO, it is necessary to select photocatalysts with better matching energy band structures to form a Z-scheme structure.

$CuBi_2O_4$(CBO), a novel Bi-based photocatalyst with a relatively negative CB potential and narrow band gap (1.7 eV), has attracted much attention due to its wide light absorption range and high light absorption efficiency. At the same time, it also has the disadvantage of a high carrier recombination rate [28–30]. Hence, $CuBi_2O_4$ can be selected as suitable semiconductors to construct a heterojunction structure with a matched energy band structure.

$Sn_3O_4$(SNO) is also a promising candidate for the construction of Z-scheme heterojunctions due to the ideal band gap (2.5 eV) and relatively negative CB potential [31–33]. Therefore, we can speculate that the construction of a dual Z-scheme heterojunction structure CBS can promote carrier separation while retaining redox capability, which is a feasible method to improve photocatalytic performance.

In this paper, we successfully synthesized Z-scheme CBS photocatalysts using the hydrothermal method. Then, the photocatalytic performance of the CBS composite was tested via degradation of tetracycline under visible light irradiation. Heterojunction materials can effectively broaden the spectral response range of the photocatalyst, promote carrier separation, inhibit recombination, and enhance photocatalytic activity. Finally, the possible mechanism of photocatalytic degradation of tetracycline was proposed based on our analysis.

## 2. Results and Discussion

### 2.1. Characterization

The phase of the BSO, CBO, SNO, and CBS-2 composites was characterized via XRD. Figure 1 displays the XRD patterns of pure BSO, CBO, SNO, and CBS-2. For pure BSO, the distinct diffraction peaks at 28.8°, 33.4°, 48.0°, 56.9°, 59.7°, and 77.6° are in good agreement with the (222), (400), (440), (622), (444), and (662) crystal planes of BSO (JCPDS NO. 87-0284). For pure CBO, the principal peaks at 14.7°, 20.9°, 28.0°, 30.7°, 33.2°, 37.4°, 43.2°, 45.1°, 46.7°, 47.8°, 53.0°, 55.6°, 57.9°, 60.7°, 64.3°, 66.0°, 73.0°, 74.4°, and 78.2° are consistent with the (110), (200), (211), (220), (310), (202), (222), (330), (411), (420), (213), (332), (422), (521), (512), (413), (541), (602), and (622) crystal planes of CBO (JCPDS NO. 72-0493). For pure SNO, the main peaks at 27.0°, 32.3°, 37.0°, 50.0°, and 51.7° are well-matched with the (111), (−121), (130), (−301), and (−1−32) crystal planes of $Sn_3O_4$ (JCPDS NO. 16-0737). There are no extra peaks from the $SnO_2$ or SnO phase appearing in the XRD pattern of SNO, implying that the as-synthesized sample is pure SNO. The sharp feature peaks of the pure sample represent high crystallinity, and no extra impurity peaks indicate its high purity. Because of the low content and overlapping characteristic peaks, the main diffraction peaks of the composite samples are similar to BSO; however, they are consistent with the (111) crystal plane of SNO at 27° and the (202) crystal plane of CBO at 37.5°, which proves the coexistence of BSO, CBO, and SNO phases in the CBS composites. In summary, the double Z-scheme CBS-2 was successfully obtained.
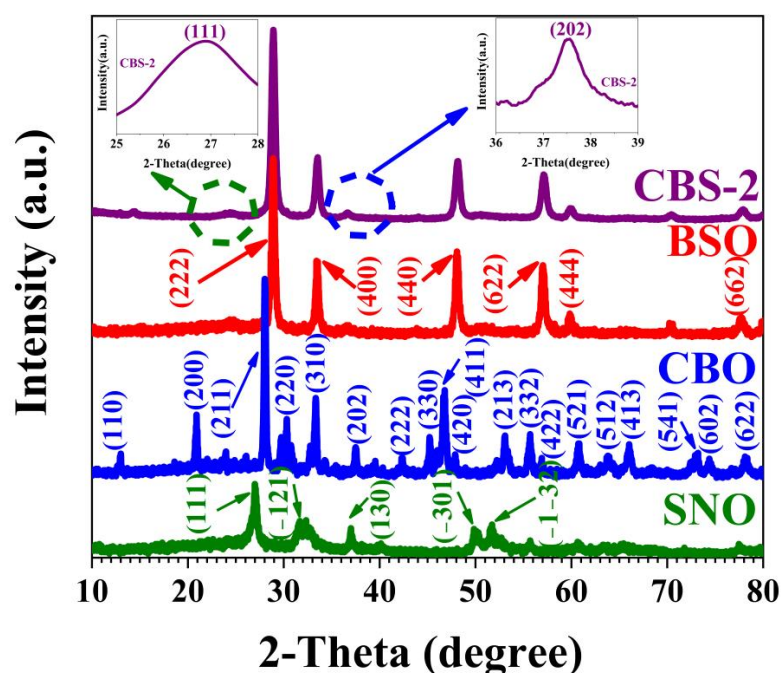
**Figure 1.** XRD patterns of BSO, CBO, SNO, and CBS-2 composite samples.

TEM and HRTEM indicate the morphology and crystalline structure of the as-prepared photocatalyst. As shown in Figure 2a–c, pure BSO is composed of many microspheres, CBO presented rod-like morphology, and SNO exhibited the flower structure. Figure S1 shows the TEM image of composite CBS-2, in which CBO and SNO can be identified; parts of BSO microspheres were successfully distributed on the surface of SNO and CBO due to the in situ generation method. In Figure 2d, we can display the 0.31 nm crystal lattice corresponding to the (222) crystal plane of BSO, the 0.24 nm crystal lattice corresponding to the (211) crystal plane of CBO, and the 0.32 nm crystal lattice corresponding to the (111) crystal plane of SNO, respectively. BSO, CBO, and SNO are observed to be closely combined. Therefore, the TEM and HRTEM images prove the existence of CBO and SNO in the composite material and they are in close connection with the basal BSO material and jointly construct the heterojunction structure.
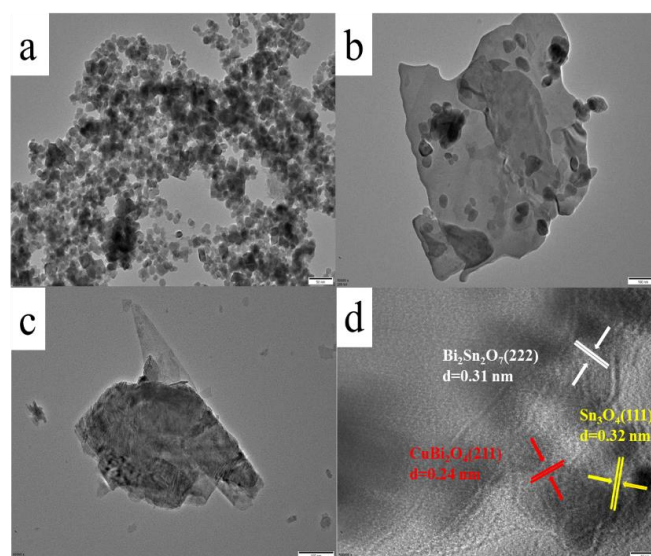


**Figure 2.** TEM images of (**a**) BSO, (**b**) CBO, (**c**) SNO, (**d**) HRTEM image of CBS-2.

The micro-strain variation is linked with the crystallite size changes, and $\delta$ ($\delta = 1/D^2$) has a direct impact on lattice imperfection. We can calculate the average crystalline size from the XRD results using the Debye–Scherrer formula [34]:

$$D = K\,\lambda/\beta\,cos\theta$$

The average crystalline size of BSO, CBO, SNO, and CBS-2 is about 17.5 nm, 11.6 nm, 10.3 nm, and 17.2 nm, respectively, which also supported TEM results.

XPS testing was used to further confirm the elemental composition and valence state of the prepared materials. The XPS survey spectra of BSO and CBS-2 are reproduced in Figure S2. The BSO contains Bi, Sn, and O elements, while the composite samples contain Bi, Sn, O, and Cu elements, which suggest the coexistence of CBO in CBS-2. In Figure 3a, the Bi 4f high-resolution spectrum, the peaks near 164.7 eV and 159.4 eV correspond to the orbital binding energies of Bi $4f_{5/2}$ and Bi $4f_{7/2}$, respectively, which proves that in BSO and composites, Bi exists in the form of $Bi^{3+}$ [35,36]. In Figure 3b, the Sn 3d high-resolution spectrum of BSO, the orbital binding energies of $3d_{3/2}$ and $3d_{5/2}$ correspond to the peaks near 486.9 eV and 495.6 eV, respectively, which proves that it exists in the form of $Sn^{4+}$ [37]. In the Sn 3d high-resolution spectrum of the complex, $3d_{3/2}$ and $3d_{5/2}$ can be deconvoluted into four peaks, indicating that there is more than one valence state of Sn in the sample. The peaks near 486.8 eV and 495.5 eV correspond to $Sn^{4+}$, and the peak at 486.3 eV and 494.8 eV corresponds to $Sn^{2+}$ [38]. In Figure 3c, the Cu 2p high-resolution spectrum, the binding energies of Cu $2p_{3/2}$ and Cu $2p_{1/2}$ peaks are 934.7 eV and 954.8 eV, representing $Cu^{2+}$ [39]. In Figure 3d, the O 1s high-resolution spectrum, the binding energy of 529.8 eV corresponds to the Bi-O bond, 531.7 eV corresponds to the Sn-O bond, and 532.2 eV corresponds to the surface adsorbed oxygen [40].
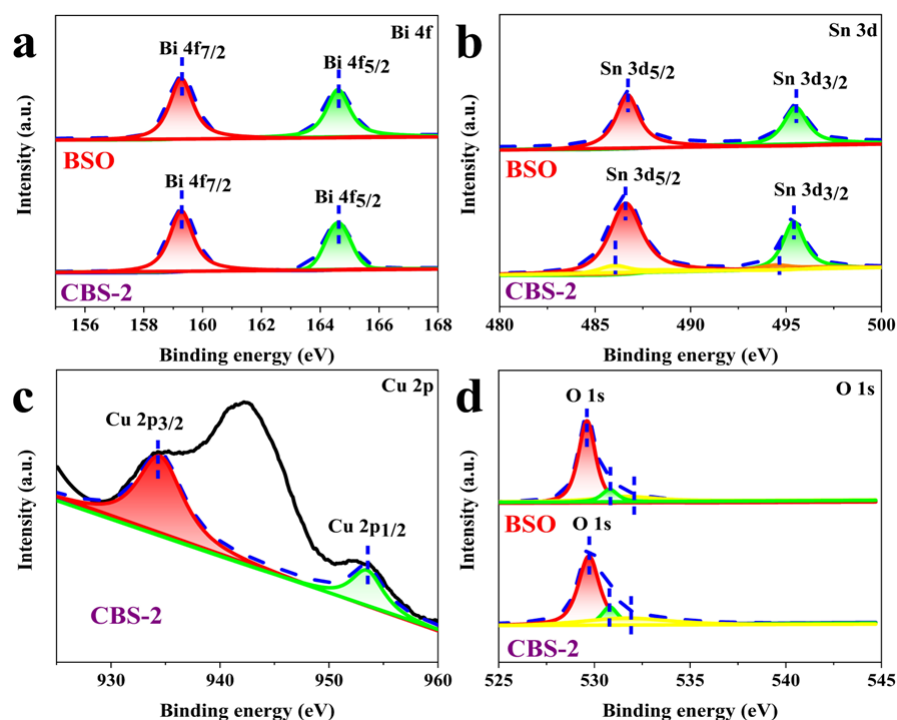


**Figure 3.** XPS spectra of (**a**) Bi 4f, (**b**) Sn 3d, (**c**) Cu 2p, (**d**) O 1s.

We measured the average particle size using dynamic light scattering. The average particle size of BSO, CBO, and SNO is 1142 nm, 463.1 nm, and 287.6 nm, CBO/BSO is 522.1 nm, and CBS-1, CBS-2, and CBS-3 is 207.3 nm, 208.6 nm, and 211.5 nm, respectively, which is similar to the TEM images. Although the average crystalline size of CBS-2 is similar

to that of BSO, its average particle size is smaller, and the particles are more dispersed, which means that it has a larger specific surface area and more active sites.

The light absorption range of a photocatalyst is closely related to its photocatalytic capacity. The as-prepared samples were characterized via UV–Vis diffuse reflectance spectroscopy to investigate their optical absorption characteristics. According to Figure 4a, the absorption edge range of BSO is about 450 nm–500 nm, CBO is about 750 nm–800 nm, and that of SNO is about 500–550 nm. The composite photocatalyst CBS-2 is slightly red-shifted on the base of pure BSO, which confirms the visible-light response ability of CBS-2. Their band gaps can be obtained from the following formula [41]:

$$Ah\nu = A(h\nu - Eg)^{n/2}$$

where $\alpha$, $h$, $\nu$, and $Eg$ represent proportionality constant, Planck constant, and optical frequency, and $n$ is related to semiconductor type. According to the literature, BSO and SNO are indirect semiconductors, $n = 4$, and CBO is a direct semiconductor, $n = 1$ [35,39,42]. Therefore, it can be roughly deduced that the $Eg$ of BSO is 2.76 eV, the $Eg$ of CBO is 1.55 eV, and the $Eg$ of SNO is 2.39 eV. The calculation results are shown in Figure 4b,c, which is consistent with the previous literature.
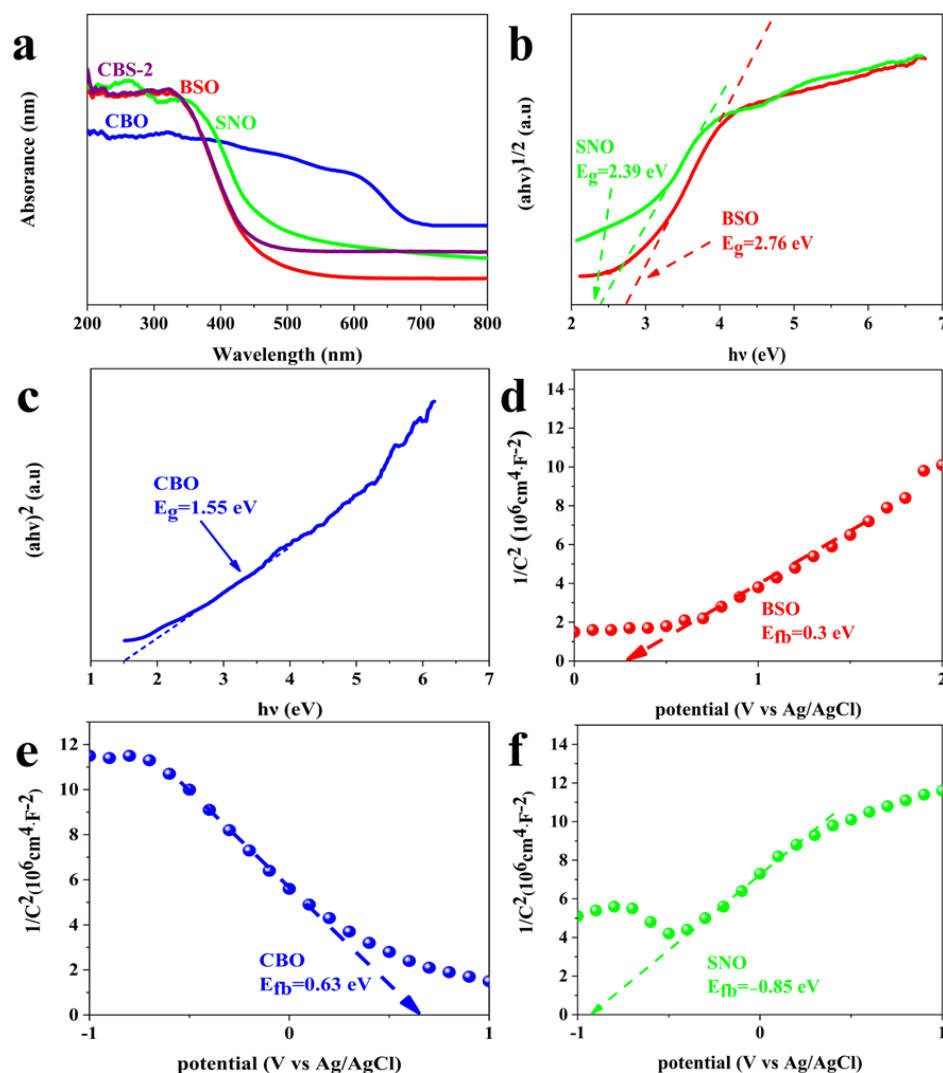


**Figure 4.** (**a**) UV-Vis diffuse reflectance absorption spectra of BSO, CBO, SNO, and CBS-2, (**b**) plots of $(\alpha h\nu)^{1/2}$ versus $h\nu$ of BSO and SNO, (**c**) plots of $(\alpha h\nu)^2$ versus $h\nu$ of CBO, Motte-Schottky (M-S) plots of (**d**) BSO, (**e**) CBO and (**f**) SNO.

In addition, the band structure of photocatalysts is also one of the important factors affecting the photocatalytic ability of photocatalysts. We can implement the Mott–Schottky (M–S) curves to measure its flat-band potential, then estimate the position of the energy band of the photocatalytic materials. As illustrated in Figure 4d–f, the slopes of BSO and SNO tangents are positive, indicating that both BSO and SNO are *n*-type semiconductors. The slope of the CBO tangent is negative, indicating that CBO is a *p*-type semiconductor. The tangents of BSO, CBO, and SNO are extended, and the flat band potential (*Efb*) of BSO, CBO, and SNO is about 0.3 eV, 0.63 eV, and −0.85 eV, respectively (*Efb* | $_{Ag/AgCl}$). We can obtain standard hydrogen electrode values by using the following equation [43]:

$$Efb\,|\,_{NHE} = Efb\,|\,_{Ag/AgCl} + 0.197$$

The minimum value of the n-type conduction band (CB) semiconductor is about 0.1 eV higher than the flat-band potential, and the maximum value of the *p*-type semiconductor valence band (VB) is about 0.1 eV lower than the flat-band potential. Therefore, the $E_{CB}$ values of BSO and SNO are calculated as 0.40 eV and −0.75 eV, and the $E_{VB}$ values of CBO are calculated as 0.93 eV. Then, we calculate their corresponding potential according to the following formula:

$$E_{VB} = E_{CB} + E_g$$

Therefore, it can be concluded that the $E_{VB}$ values of BSO and SNO are calculated as 3.16 eV and 1.64 eV, and the $E_{VB}$ values are calculated as −0.92 eV [30,40,44].

## 2.2. Photocatalytic Activity

We tested the photocatalytic performance of the photocatalyst via the degradation efficiency of the model pollutant, tetracycline solution, under visible light. Results are as shown in Figure 5a,b: pure samples reveal poor photocatalytic activities, the photocatalytic activities of BSO, CBO, and SNO are only 56.2%, 10.3%, and 5%, and the CWO/BSO heterojunction material showed higher photocatalytic activity than pure samples, but lower than the CBS Z-scheme heterojunction under the same conditions. The best photocatalytic activity of CBS-2 is 89.7% under the same conditions. This may be because, due to the increase in CBO and SNO content, more heterojunction structures were generated, thus improving the photocatalytic activity. However, with the further increase in CBO and SNO content, the photocatalytic activity of the composite decreases, which may be because the decrease in active reaction sites reduces the optical adsorption capacity of the composite catalyst [45,46].
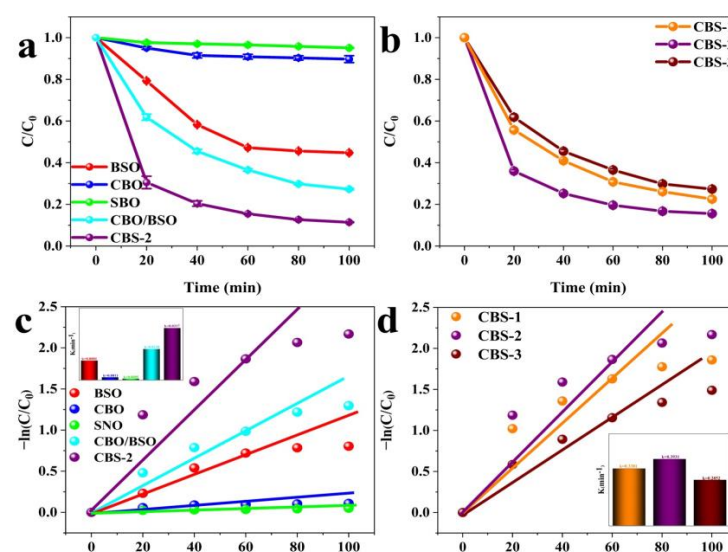


**Figure 5.** *Cont.*
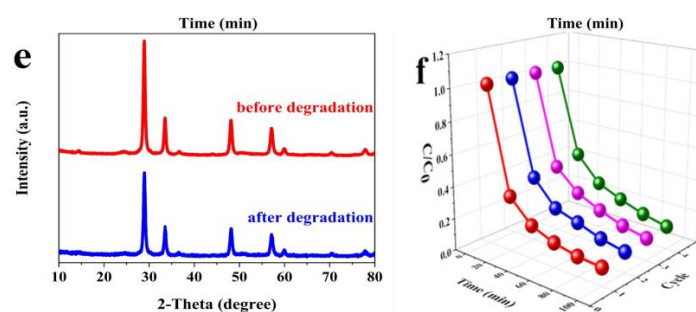
**Figure 5.** (**a**) Dynamic degradation curves of TC by different samples under visible light illumination, (**b**) dynamic degradation curves of TC by CBS with different composite proportions, (**c**) the apparent kinetic constants corresponding to BSO, CBO, SNO, CBO/BSO, and CBS-2 TC degradation, (**d**) the apparent kinetic constants corresponding to CBS with different composite proportions TC degradation, (**e**) XRD patterns comparison before and after photocatalytic cycling, (**f**) photocatalytic cycling tests for TC degradation.

The comparison of the tetracycline degradation activity of CBS-2 and other photocatalytic materials is shown in Table 1.

**Table 1.** Comparison of the photocatalytic performance of different photocatalysts.

| Photocatalysts | Quality | TC Content | Light Source | Efficiency | Ref |
|---|---|---|---|---|---|
| $Bi_2Sn_2O_7/UiO$-66-$NH_2$ | 10 mg | 50 mL 25 mg/L | 400 W Xe lamp $\lambda > 400$ nm | 86% (120 min) | [47] |
| $Bi_2Sn_2O_7/Bi_2MoO_6$ | 35 mg | 100 mL 20 mg/L | 300 W Xe lamp $\lambda > 400$ nm | 99.4% (100 min) | [37] |
| $BiOBr/Bi_2Sn_2O_7$ | 20 mg | 20 mL 20 mg/L | 500 W Xe lamp $\lambda > 400$ nm | 51.3% (80 min) | [48] |
| $C_3N_4/Bi_2Sn_2O_7$ | 200 mg | 100 mL 20 mg/L | 300 W Tungsten Halogen lamp | 80.4% (90 min) | [49] |
| $SnO_2/Bi_2Sn_2O_7$ | 25 mg | 50 mL 20 mg/L | 300 W Xe lamp $\lambda > 400$ nm | 88.4% (180 min) | [50] |
| $Ag/Bi_2Sn_2O_7$-$C_3N_4$ | 200 mg | 200 mL 20 mg/L | 400 W Tungsten Halogen lamp | 89.1% (90 min) | [51] |
| $BiOBr/Bi_2Sn_2O_7$ | 10 mg | 30 mL 10 mg/L | 300 W Xe lamp $\lambda > 400$ nm | 50.4% (60 min) | [27] |
| $Ag@ZnO/Bi_2Sn_2O_7$ | 50 mg | 100 mL 10 mg/L | 300 W Xe lamp $\lambda > 400$ nm | 74% (60 min) | [20] |
| $Nd_2Sn_2O_7/Bi_2Sn_2O_7/Ag_3PO_4$ | 20 mg | 50 mL 15 mg/L | 45 W lamp $\lambda > 400$ nm | 97.1% (120 min) | [23] |
| $CuBi_2O_4/Bi_2Sn_2O_7/Sn_3O_4$ | 50 mg | 100 mL 5 mg/L | 300 W Xe lamp $\lambda > 400$ nm | 89.7% (100 min) | This work |

Figure 5c,d shows the apparent kinetic constants of different catalysts degrading tetracycline solution, which can be calculated according to the following equation [52]:

$$-ln(C_t/C_0) = kt$$

$C_0$ represents the concentration of the tetracycline solution before illumination starts after dark treatment, and $C_t$ represents a concentration of the tetracycline solution at t min. As illustrated in Figure 5c,d, the apparent rate constant values of BSO, CBO, and SNO are 0.1674, 0.0195, and 0.0089 $min^{-1}$, that of CBO/BSO is 0.2572 $min^{-1}$, and those of CBS-1, CBS-2, and CBS-3 are 0.3381, 0.3931, and 0.2852 $min^{-1}$. The composite CBS-2 possessed the highest k value, about 2.34, 20.16, and 44.17 times those of pure BSO, CBO, and SNO.

The $R^2$ value of BSO, CBO, and SNO are 0.8455, 0.8397, and 0.994, that of CBO/BSO is 0.967, and those of CBS-1, CBS-2, and CBS-3 are 0.9389, 0.9475, and 0.9785. The $R^2$ value of most photocatalysts is greater than 0.9, except for BSO and CBO.

In addition to photocatalytic activity, the stability and reusability of photocatalysts are also key considerations restricting their applications [53]. XRD tests were carried out before and after the photocatalytic cycling experiment, respectively. Figure 5e shows that the crystal structure of the photocatalyst has no obvious change after four cycles of photocatalysis. In Figure 5f, the degradation efficiency remained stable after four cycles, the degradation rates of the four repeated experiments were 88.9%, 87.2%, 86.1%, and 85.6%, and the photocatalytic activity of CBS-2 was only slightly decreased by about 4.3% after four photocatalytic cycling experiments. The decrease in activity may be due to the adsorption of TC by the active site of the catalyst. In short, the composite material can be reused.

### 2.3. Photocatalytic Mechanism

To investigate the transfer and separation efficiency of photogenerated carriers, photocurrent cycle experiments were carried out on samples. A high photocurrent intensity reflects high separation efficiency [54]. As shown in Figure 6a, the photocurrent intensity of CBS-2 is higher than that of the pure samples, which indicates that the CBS-2 composite material has the strongest carrier transfer and separation efficiency.
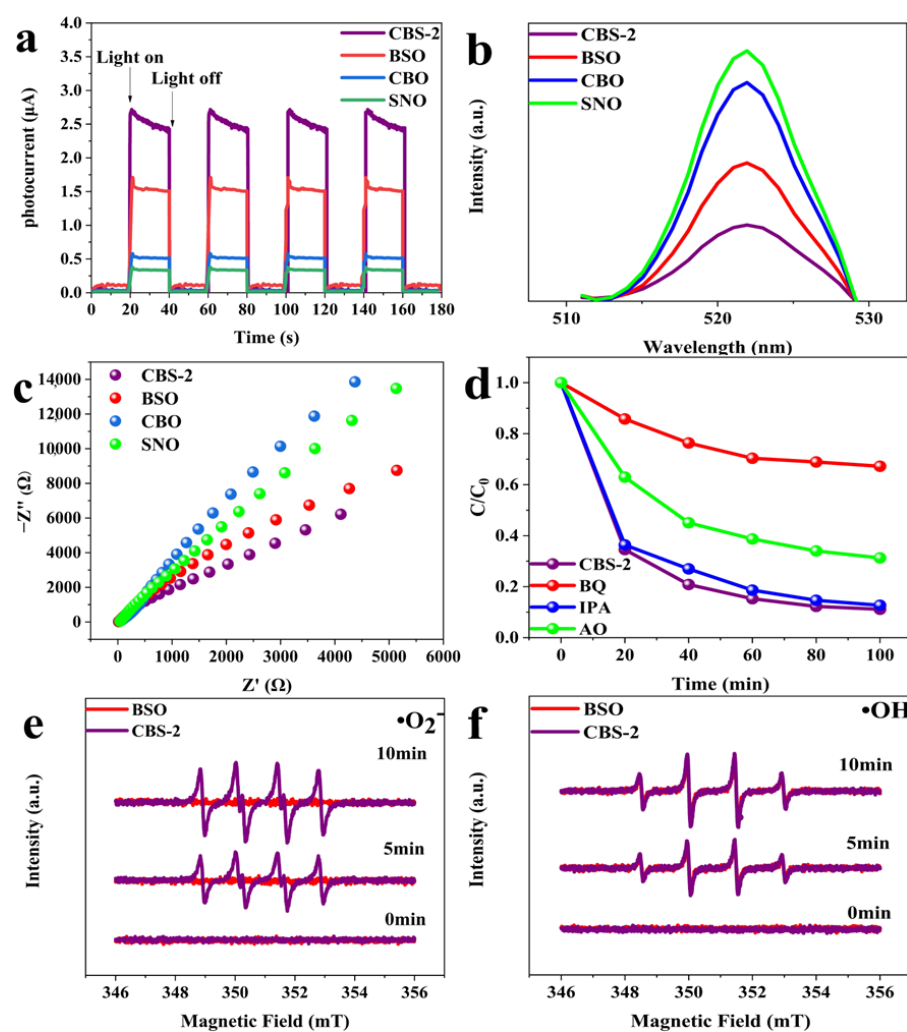


**Figure 6.** (**a**) Transient photocurrent response of BSO, CBO, SNO, and CBS-2 composite samples, (**b**) photoluminescence spectra of BSO, CBO, SNO, and CBS-2 composite samples, (**c**) electrochemical impedance spectroscopy of BSO, CBO, SNO, and CBS-2, (**d**) effects of different trapping agents on TC degradation of CBS-2, (**e**) the ESR signals of $\bullet O_2^-$ of pure BSO and CBS-2 photocatalysts, (**f**) the ESR signals of $\bullet OH$ of pure BSO and CBS-2 photocatalysts.

The relatively weak PL intensity represents a high separation efficiency [55]. In Figure 6b, the high PL emission peaks of BSO, CBO, and SNO imply a high photogenerated carrier recombination rate, while CBS-2 shows a lower emission peak. Constructing a double Z-scheme heterostructure between BSO, CBO, and SNO, the carrier separation efficiency is higher than that of the pure sample, and the recombination of electron–hole pairs can be suppressed effectively so that the composite material exhibits enhanced photocatalytic activity.

To confirm the difference in the charge transfer separation efficiency and impedance between different samples, electrochemical impedance spectroscopy (EIS) tests were performed on BSO, CBO, SNO, and the composite material. The smaller radius of the circle in the diagram means lower resistance, and faster electron migration rate [56]. Figure 6c shows the relative radius of the pure and composite photocatalyst, sorted by size as CBO > SNO > BSO > CBS-2.

According to characterization results, due to the successful construction of the heterojunction, the average particle size was reduced, the optical absorption range of CBS was widened, the carrier separation efficiency was improved, and the photogenerated carrier recombination rate was reduced; therefore, the photocatalytic activity was significantly improved.

To inspect the main active radicals in the photocatalytic process of the CBS-2 composite, we performed a radical trapping experiment. The experimental results are shown in Figure 6d: the addition of IPA has almost no effect on the degradation efficiency, but the degradation efficiency is significantly inhibited by the addition of BQ, and the addition of AO also has a certain inhibitory effect on the degradation efficiency. The degradation efficiency dropped slightly from 88.9% to 32.8% and 68.8% when BQ and AO were added. These results indicate that $\bullet O_2^-$ and $h^+$ act synergistically in the photocatalytic process of CBS-2, of which $\bullet O_2^-$ is more important.

To elucidate the possible mechanism, ESR characterization and trapping experiments were used to detect the main active radicals. From Figure 6e, $\bullet O_2^-$ characteristic signals of pure BSO cannot be obtained under visible light or in the dark, while that of CBS-2 can, which illustrates the presence of $\bullet O_2^-$ and its participation in the photocatalytic process. As shown in Figure 6f, both BSO and CBS-2 can receive $\bullet OH$ characteristic signals after irradiation. Trapping experiments also illustrate that $h^+$ and $\bullet O_2^-$ play critical roles in the degradation of TC.

Figure 7 illustrates the possible mechanism of the photodegradation of TC. The double Z-scheme photocatalytic is constructed with BSO, CBO, and SNO. Under visible light, they are all motivated to generate photoproduced electron–hole pairs. According to the classic type II heterojunction transfer mechanism, the CB of BSO (0.4 eV) is more positive, and the electrons on the CB of CBO and SNO will transfer to the CB of BSO. Meanwhile, the $h^+$ shift from BSO to CBO and SNO occurs because of the more positive VB of BSO. The CB of BSO is more positive than $O_2/\bullet O_2^-$ (−0.33 eV), and the VB of CBO and SNO is more negative than $H_2O/\bullet OH$ (2.27 eV), so it is impossible to generate $\bullet O_2^-$ thermodynamically. However, that inference contrasts with the results of trapping experiments and ESR analysis. It can be inferred that the photogenerated carrier migration follows a Z-scheme mechanism. When BSO, CBO, and SNO are motivated to generate holes and electrons, the electrons on the CB of BSO recombine with the holes on the VB of CBO and SNO, which not only retains the $e^-$ of CBO and SNO with stronger reduction and the $h^+$ of BSO with oxidation ability in the CBS-2 system but also maintains the separation of charge carriers. Some holes on the VB of BSO can directly degrade the TC solution, and others can react with $H_2O$ to generate $\bullet OH$ to further degrade the TC solution. In addition, the electrons on the CB of CBO and SBO can convert the adsorbed oxygen into $\bullet O_2^-$, thereby further oxidatively degrading the TC solution. The construction of the double Z-scheme mechanism improves the efficiency of carrier separation and migration while retaining the strong redox ability of the catalyst, thereby enhancing the photocatalytic performance of the composite.
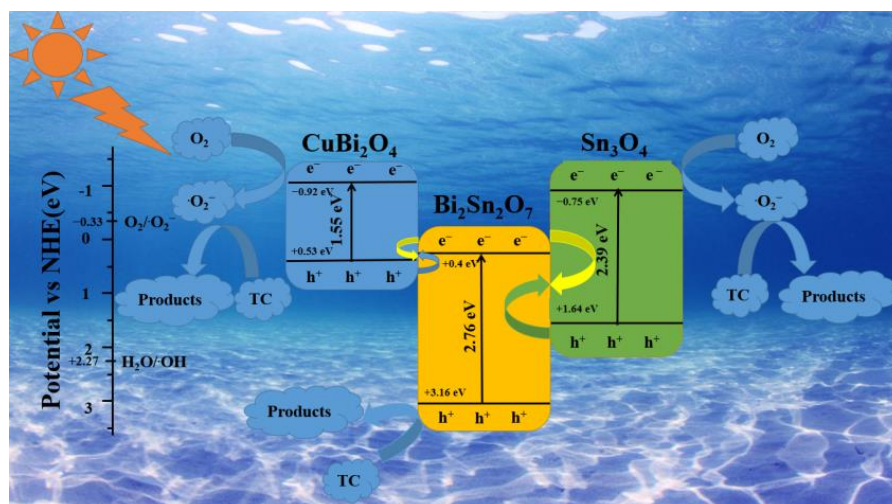
**Figure 7.** Possible mechanism of TC degradation by double Z-scheme CBS-2 composite photocatalyst under visible light.

## 3. Experimental

### 3.1. Preparation of Photocatalysts

#### 3.1.1. Synthesis of BSO

Based on previous reports, $Bi_2Sn_2O_7$ was synthesized using a simple hydrothermal method [40]. Generally, $SnCl_4 \cdot 5H_2O$ (2.80 g) was dissolved in 80 mL $H_2O$, $Bi(NO_3)_3 \cdot 5H_2O$ (3.88 g) was added slowly to it under rapid stirring, and 80 mL 2 M NaOH solution was gradually dropped into it afterward. Then, the suspension was transferred to a 200 mL stainless steel hydrothermal kettle and kept at 180 °C for 24 h, filtered and cleaned with a large amount of water and absolute ethanol after the reaction to separate the powder from the liquid, and finally dried at 60 °C to collect the yellow powder. The material is recorded as BSO.

#### 3.1.2. Synthesis of CBO/BSO

Firstly, $Bi(NO_3)_3 \cdot 5H_2O$ (2.42 g), $Cu(NO_3)_2 \cdot 3H_2O$ (0.60 g) and NaOH (0.87 g) were distracted into 80 mL water and stirred for 3 h. Then, a certain amount of BSO was added and stirred for 1 h. Finally, the mixed solution was transferred to a 100 mL stainless steel hydrothermal kettle and kept at 180 °C for 24 h, filtered and cleaned with a large amount of water and absolute ethanol after the reaction to separate the powder from the liquid, and finally dried at 60 °C for use. The mass ratio between CBO and BSO in the prepared samples was 1%, which was denoted as CBO/BSO. Pure CBO samples were prepared through the same protocol without the addition of BSO [30].

#### 3.1.3. Synthesis of CBS

We fully dissolved $Na_3C_6H_5O_7 \cdot 2H_2O$ (2.94 g) and $SnCl_2 \cdot 2H_2O$ (0.90 g) in 10 mL of water, gradually dropped 10 mL of 0.2 M NaOH into it under continuous stirring, added a certain amount of CBO/BSO after stirring for half an hour, and stirred for another hour. The suspension was put into a 50 mL hydrothermal reactor, and reacted at 180 °C for 12 h; after cooling, the product was filtered and washed with a large amount of water and absolute ethanol, and finally dried at 60 °C for later use. The sample with a mass of CBO accounting for 1% of the total mass and a mass of SNO accounting for 1% of the total mass was labeled as CBS-1, the sample with a the mass of CBO accounting for 1% of the total mass and a mass of SNO accounting for 2% of the total mass was labeled as CBS-2, and the sample with a mass of CBO accounting for 2% of the total mass and a mass of SNO accounting for 5% of the total mass was labeled as CBS-3. Pure SNO samples were prepared through the same protocol without the addition of CBO/BSO [44].

### 3.2. Characterization Methods

The composition and crystallinity characteristics of the as-prepared photocatalysts were measured with an X-ray powder diffractometer (Shimaduz-6100, Kyoto, Japan) at a scan rate of $10°/min$ from $10°$ to $80°$. Transmission electron microscope (TEM) images and high-resolution transmission electron microscope (HRTEM) images were used to observe the size and microstructure of the photocatalytic materials. X-ray photoelectron spectroscopy (XPS) was carried out on a Thermo (Waltham, USA) ESCALAB 250Xi spectrometer, which was devoted to analyzing the elemental composition and its valence state in the photocatalysts. The particle size of the characterized photocatalysts was analyzed with a Malvern Zetasizer Nano ZS90. Taking $BaSO_4$ as the reflection standard to test the absorption edge of the sample, the UV-Vis diffuse reflectance spectra (UV-DRS) were performed on a Shimadzu UV-3600 spectrophotometer in the range 200 nm to 800 nm. Electrochemical tests were obtained with a CHI-660D electrochemical workstation. We used 0.1 M sodium sulfate solution as an electrolyte solution in photoelectric tests. The sample electrode played the role of the working electrode. In the beginning, 10 mg of photocatalysts and microscale Nafion were uniformly dispersed in a minute quantity of ethanol via ultrasonic treatment. Then, the mixture was spread evenly on one square centimeter area of FTO glass. Finally, it was dried at 120 °C for 2 h. Photoluminescence (PL) spectra were characterized using a fluorescence spectrometer (Cary Eclipse, Agilent, Santa Clara, CA, USA) at an excitation wavelength of 520 nm. The electron paramagnetic resonance spectra of the as-prepared photocatalysts were characterized with the JES FA200 EPR Spectrometer. Radicals were measured via electron spin resonance (ESR, EOL JES-FA200 EER) using 5,5-dimethyl-1-pyrroline oxynitride (DMPO) as a spin trap.

### 3.3. Photocatalytic Evaluation

The photocatalytic performance of the samples was evaluated by calculating the degradation rate of tetracycline under 300 W xenon lamp irradiation with a filter ($\lambda > 400$ nm). Firstly, an aqueous solution containing tetracycline (100 mL, 5 ppm) and 50 mg photocatalyst was stirred uniformly in the dark for half an hour to reach adsorption–desorption equilibrium. Then, it was placed in a 250 mL cylindrical quartz reactor cooled with cold water circulating outside the reactor. The stirrer was used to ensure that the suspension stayed homogeneous during the photocatalytic reaction, removing the supernatant from the reactor at intervals. Finally, after sampling and centrifugation, the supernatant was filtered through a 0.22 m filter membrane and then quantitatively analyzed via high-performance liquid chromatography. The mobile phase was methanol, acetonitrile, and 0.01 M oxalic acid in a 1:2:7 volume ratio.

## 4. Conclusions

In summary, we synthesized a double Z-scheme CBS-2 photocatalyst using the in situ generation method and found that it exhibited stronger photocatalytic performance than the constituent parts. The best sample, CBS-2 composite, achieved 89.7% degradation efficiency of TC solution under visible light irradiation. The value of k was about 2.34, 20.16, and 44.17 times those of BSO, CBO, and SNO. The active species $\bullet O_2^-$ and $h^+$ all participated in the removal of TC, in which $\bullet O_2^-$ plays a major role. Considering the results of the capture experiment and ESR characterization, the electron transfer pattern follows the Z-scheme heterojunction. The Z-scheme heterojunction suppressed the recombination of photogenerated carriers and retained the strong redox ability of the catalyst. Furthermore, it possessed good stability after cycle experiments. Hence, the dual Z-scheme CBS-2 photocatalyst has a huge application prospect for removing wastewater under visible light. In a word, we advance the study of Z-heterojunction photocatalysis, then provide a new method to improve the photocatalytic activity of BSO, and finally find a photocatalytic material that can degrade tetracycline efficiently.

## References

1. He, Y.; Gao, M.; Zhou, Y.; Zhou, Y. Efficient photocatalytic remediation of typical antibiotics in water via $Mn_3O_4$ decorated carbon nitride nanotube. *Chemosphere* **2023**, *311*, 136925. [CrossRef] [PubMed]
2. Wang, B.; Li, Z.; Ma, H.; Zhang, J.; Jiao, L.; Hao, H.; Liu, E.; Xu, L.; Wang, C.; Zhou, B. Dynamic construction of self-assembled supramolecular $H_{12}SubPcB$-OPhCOOH/$Ag_3PO_4$ S-scheme arrays for visible photocatalytic oxidation of antibiotics. *Appl. Catal. B Environ.* **2022**, *318*, 121882. [CrossRef]
3. Yu, J.; Zhang, P.; Zhang, Y.; Sun, K.; Shi, X.; Li, L. The preparation of conjugated microporous polymer composite materials with montmorillonite template and its improvement in photocatalytic degradation for multiple antibiotics. *Appl. Clay Sci.* **2023**, *231*, 106752. [CrossRef]
4. Chin, J.Y.; Ahmad, A.L.; Low, S.C. Evolution of photocatalytic membrane for antibiotics degradation: Perspectives and insights for sustainable environmental remediation. *J. Water Process Eng.* **2023**, *51*, 103342. [CrossRef]
5. Hu, X.; Zhang, Y.; Chen, Z.; Gao, Y.; Teppen, B.; Boyd, S.A.; Zhang, W.; Tiedje, J.M.; Li, H. Tetracycline accumulation in biofilms enhances the selection pressure on Escherichia coli for expression of antibiotic resistance. *Sci. Total Environ.* **2023**, *857*, 159441. [CrossRef]
6. Zhang, Y.; Li, Y.; Xu, W.; Cui, M.; Wang, M.; Chen, B.; Sun, Y.; Chen, K.; Li, L.; Du, Q. Filtration and adsorption of tetracycline in aqueous solution by copper alginate-carbon nanotubes membrane which has the muscle-skeleton structure. *Chem. Eng. Res. Des.* **2022**, *183*, 424–438. [CrossRef]
7. Varadharajan, V.; Senthilkumar, D.S.; Senthilkumar, K.; Sundramurthy, V.P.; Manikandan, R.; Senthilarasan, H.; Ganesan, H.; Kesavamoorthy, I.; Ramasamy, A. Process modeling and toxicological evaluation of adsorption of tetracycline onto the magnetized cotton dust biochar. *J. Water Process Eng.* **2022**, *49*, 103046. [CrossRef]
8. Han, K.; Liu, Y.; Hu, J.; Jia, J.; Sun, S. Effect of live and inactivated Chlamydomonas reinhardtii on the removal of tetracycline in aquatic environments. *Chemosphere* **2022**, *309*, 136666. [CrossRef] [PubMed]
9. Hu, P.; Shao, J.; Qian, G.; Adeleye, A.S.; Hao, T. Removal of tetracycline by aerobic granular sludge from marine aquaculture wastewater: A molecular dynamics investigation. *Bioresour. Technol.* **2022**, *355*, 127286. [CrossRef]
10. Das, S.; Ahn, Y.-H. Synthesis and application of CdS nanorods for LED-based photocatalytic degradation of tetracycline antibiotic. *Chemosphere* **2022**, *291*, 132870. [CrossRef] [PubMed]
11. Wang, Y.; Wu, X.; Liu, J.; Zhai, Z.; Yang, Z.; Xia, J.; Deng, S.; Qu, X.; Zhang, H.; Wu, D. Mo-modified band structure and enhanced photocatalytic properties of tin oxide quantum dots for visible-light driven degradation of antibiotic contaminants. *J. Environ. Chem. Eng.* **2022**, *10*, 107091. [CrossRef]
12. Pei, Z.; Guo, H.; Zhu, L.; Li, C.; Fu, Z.; Xu, J. Photocatalytic degradation of various antibiotics under visible light irradiation by CdS-doped $SiO_2$@ BiOX (X= Br, Cl) prepared by mixed solvothermal method. *Mater. Sci. Eng. B* **2023**, *287*, 116134. [CrossRef]
13. Pan, J.; Wang, L.; Shi, Y.; Li, L.; Xu, Z.; Sun, H.; Guo, F.; Shi, W. Construction of nanodiamonds/UiO-66-$NH_2$ heterojunction for boosted visible-light photocatalytic degradation of antibiotics. *Sep. Purif. Technol.* **2022**, *284*, 120270. [CrossRef]
14. Mukhtar, F.; Munawar, T.; Nadeem, M.S.; ur Rehman, M.N.; Khan, S.A.; Koc, M.; Batool, S.; Hasan, M.; Iqbal, F. Dual Z-scheme core-shell PANI-$CeO_2$-$Fe_2O_3$-NiO heterostructured nanocomposite for dyes remediation under sunlight and bacterial disinfection. *Environ. Res.* **2022**, *215*, 114140. [CrossRef] [PubMed]
15. Munawar, T.; Nadeem, M.S.; Mukhtar, F.; Manzoor, S.; Ashiq, M.N.; Batool, S.; Hasan, M.; Iqbal, F. Multifunctional dual Z-scheme heterostructured $Sm_2O_3$-$WO_3$-$La_2O_3$ nanocomposite: Enhanced electrochemical, photocatalytic, and antibacterial properties. *Adv. Powder Technol.* **2023**, *34*, 104061. [CrossRef]

16. Yin, N.; Chen, H.; Yuan, X.; Zhang, Y.; Zhang, M.; Guo, J.; Zhang, Y.; Qiao, L.; Liu, M.; Song, K. Highly efficient photocatalytic degradation of norfloxacin via $Bi_2Sn_2O_7$/PDIH Z-scheme heterojunction: Influence and mechanism. *J. Hazard. Mater.* **2022**, *436*, 129317. [CrossRef] [PubMed]

17. Zhang, Y.; Di, J.; Zhu, X.; Ji, M.; Chen, C.; Liu, Y.; Li, L.; Wei, T.; Li, H.; Xia, J. Chemical Bonding Interface in $Bi_2Sn_2O_7$/BiOBr S-Scheme Heterojunction Triggering Efficient $N_2$ Photofixation. *Appl. Catal. B Environ.* **2022**, *323*, 122148. [CrossRef]

18. Zhou, J.; Fan, G.; Ruan, F.; Li, Y.; Fan, D.; Chen, Q. Construction of $Bi_2Sn_2O_7$/Ag/$Ag_3PO_4$ heterojunction and its photocatalytic degradation properties. *J. Taiwan Inst. Chem. Eng.* **2022**, *138*, 104443. [CrossRef]

19. Zhang, D.; Yang, Z.; Hao, J.; Zhang, T.; Sun, Q.; Wang, Y. Boosted charge transfer in dual Z-scheme $BiVO_4$@ $ZnIn_2S_4$/$Bi_2Sn_2O_7$ heterojunctions: Towards superior photocatalytic properties for organic pollutant degradation. *Chemosphere* **2021**, *276*, 130226. [CrossRef]

20. Wu, C.; Shen, Q.; Liu, J.; Jiang, L.; Sheng, J.; Li, Y.; Yang, H. Regulation of charge transfer in ZnO/$Bi_2Sn_2O_7$ heterojunction for enhanced photocatalytic performance towards antibiotic degradation. *J. Photochem. Photobiol. A Chem.* **2022**, *433*, 114142. [CrossRef]

21. Wu, C.; Shen, Q.; Zheng, S.; Zhang, X.; Sheng, J.; Yang, H. Fabrication of $Bi_2Sn_2O_7$@ MIL-100 (Fe) composite photocatalyst with enhanced superoxide-radical-dominated photocatalytic activity for ciprofloxacin degradation. *J. Mol. Struct.* **2022**, *1258*, 132657. [CrossRef]

22. Zhang, S.; Rong, Y.; Wei, J.; Li, Z.; Liang, T.; Yu, Z.; Zhu, H.; Wang, S.; Hou, Y. Flower-like microspheres Z-scheme $Bi_2Sn_2O_7$/NiAl-LDH heterojunction for boosting photocatalytic $CO_2$ reduction under visible light. *J. Colloid Interface Sci.* **2023**, *629*, 604–615. [CrossRef]

23. Zhu, P.; Lin, J.; Liu, M.; Duan, M.; Luo, D.; Wu, X.; Zhang, S. $Nd_2Sn_2O_7$/$Bi_2Sn_2O_7$/$Ag_3PO_4$ double Z-type heterojunction for antibiotic photodegradation under visible light irradiation: Mechanism, optimization and pathways. *Sep. Purif. Technol.* **2022**, *300*, 121897. [CrossRef]

24. Lv, D.; Zhang, D.; Pu, X.; Li, Y.; Yin, J.; Ma, H.; Dou, J. Facile synthesis of BiOBr/$Bi_2Sn_2O_7$ heterojunction photocatalysts with improved photocatalytic activities. *J. Am. Ceram. Soc.* **2016**, *99*, 3973–3979. [CrossRef]

25. Wu, X.-F.; Sun, Y.; Li, H.; Wang, Y.-J.; Zhang, C.-X.; Zhang, J.-R.; Su, J.-Z.; Wang, Y.-W.; Zhang, Y.; Wang, C. In-situ synthesis of novel pn heterojunction of $Ag_2CrO_4$-$Bi_2Sn_2O_7$ hybrids for visible-light-driven photocatalysis. *J. Alloys Compd.* **2018**, *740*, 1197–1203. [CrossRef]

26. Zhu, Z.; Xia, H.; Li, H.; Han, S. Facile Construction of $Bi_2Sn_2O_7$/g-$C_3N_4$ Heterojunction with Enhanced Photocatalytic Degradation of Norfloxacin. *Inorganics* **2022**, *10*, 131. [CrossRef]

27. Zhang, D.; Wu, M.; Hao, J.; Zheng, S.; Yang, Y.; Yao, T.; Wang, Y. Construction of Z-scheme heterojunction by coupling $Bi_2Sn_2O_7$ and BiOBr with abundant oxygen vacancies: Enhanced photodegradation performance and mechanism insight. *J. Colloid Interface Sci.* **2022**, *612*, 550–561. [CrossRef]

28. Zhang, X.; Wang, X.; Chai, J.; Xue, S.; Wang, R.; Jiang, L.; Wang, J.; Zhang, Z.; Dionysiou, D.D. Construction of novel symmetric double Z-scheme $BiFeO_3$/$CuBi_2O_4$/$BaTiO_3$ photocatalyst with enhanced solar-light-driven photocatalytic performance for degradation of norfloxacin. *Appl. Catal. B Environ.* **2020**, *272*, 119017. [CrossRef]

29. Chen, J.; Yao, L.; Chen, X.; Li, N.; Yu, C.; Zhang, Y.; Lai, Y. Hydrothermal synthesis of dendritic $CuBi_2O_4$ and its photocatalytic performance towards tetracycline degradation under different light conditions. *Mater. Sci. Semicond. Process.* **2022**, *142*, 106503. [CrossRef]

30. Shi, W.; Guo, F.; Yuan, S. In situ synthesis of Z-scheme $Ag_3PO_4$/$CuBi_2O_4$ photocatalysts and enhanced photocatalytic performance for the degradation of tetracycline under visible light irradiation. *Appl. Catal. B Environ.* **2017**, *209*, 720–728. [CrossRef]

31. Jiang, X.; Wang, M.; Luo, B.; Yang, Z.; Li, W.; Zhang, D.; Pu, X.; Cai, P. Magnetically recoverable flower-like $Sn_3O_4$/$SnFe_2O_4$ as a type-II heterojunction photocatalyst for efficient degradation of ciprofloxacin. *J. Alloys Compd.* **2022**, *926*, 166878. [CrossRef]

32. Li, S.; Liu, Z.; Qu, Z.; Piao, C.; Liu, J.; Xu, D.; Li, X.; Wang, J.; Song, Y. An all-solid-state Z-scheme $NaNbO_3$-Au-$Sn_3O_4$ photocatalyst for effective degradation of carbofuran under sunlight irradiation. *J. Photochem. Photobiol. A Chem.* **2020**, *389*, 112246. [CrossRef]

33. Li, C.; Yu, S.; Dong, H.; Liu, C.; Wu, H.; Che, H.; Chen, G. Z-scheme mesoporous photocatalyst constructed by modification of $Sn_3O_4$ nanoclusters on g-$C_3N_4$ nanosheets with improved photocatalytic performance and mechanism insight. *Appl. Catal. B Environ.* **2018**, *238*, 284–293. [CrossRef]

34. Mukhtar, F.; Munawar, T.; Nadeem, M.S.; Khan, S.A.; Koc, M.; Batool, S.; Hasan, M.; Iqbal, F. Enhanced sunlight-absorption of $Fe_2O_3$ covered by PANI for the photodegradation of organic pollutants and antimicrobial inactivation. *Adv. Powder Technol.* **2022**, *33*, 103708. [CrossRef]

35. Sun, X.; Li, J.; Wang, Y.; Zhang, Y.; Yuan, H. The g-$C_3N_4$/$Bi_2Sn_2O_7$@ PAN nanofibers: Enhanced photocatalytic activity in H2 evolution by the formation of heterojunction and in-situ growth. *Appl. Surf. Sci.* **2023**, *608*, 155228. [CrossRef]

36. Wang, J.-C.; Wang, B.; Shi, W.; Qiao, X.; Yang, X.; Zhang, L.; Zhang, W.; Li, R.; Hou, Y. Natural-sunlight-driven synchronous degradation of 4-nitrphenol and rhodamine B over S-scheme heterojunction of α-$Fe_2O_3$ nanoparticles decorated $CuBi_2O_4$ rods. *J. Environ. Chem. Eng.* **2022**, *10*, 108565. [CrossRef]

37. Li, S.; Wang, C.; Liu, Y.; Cai, M.; Wang, Y.; Zhang, H.; Guo, Y.; Zhao, W.; Wang, Z.; Chen, X. Photocatalytic degradation of tetracycline antibiotic by a novel $Bi_2Sn_2O_7$/$Bi_2MoO_6$ S-scheme heterojunction: Performance, mechanism insight and toxicity assessment. *Chem. Eng. J.* **2022**, *429*, 132519. [CrossRef]

38. Jin, C.-Z.; Yang, X.-A.; Zhai, X.-M.; Wang, S.-B.; Zhang, W.-B. ZnO/Sn$_3$O$_4$ amorphous-crystalline heterojunctions for Cr (VI) visible photocatalysis: Simple synthesis with excellent performance. *Appl. Surf. Sci.* **2023**, *608*, 155263. [CrossRef]
39. Sabri, M.; Habibi-Yangjeh, A.; Ghosh, S. Novel ZnO/CuBi$_2$O$_4$ heterostructures for persulfate-assisted photocatalytic degradation of dye contaminants under visible light. *J. Photochem. Photobiol. A Chem.* **2020**, *391*, 112397. [CrossRef]
40. Shen, J.-C.; Zeng, H.-Y.; Chen, C.-R.; Xu, S. Novel plasmonic pn heterojunction Ag-Ag$_2$CO$_3$/Bi$_2$Sn$_2$O$_7$ photocatalyst for Cr (VI) reduction. *J. Taiwan Inst. Chem. Eng.* **2021**, *120*, 106–115. [CrossRef]
41. Tang, Q.-Y.; Yang, M.-J.; Yang, S.-Y.; Xu, Y.-H. Enhanced photocatalytic degradation of glyphosate over 2D CoS/BiOBr heterojunctions under visible light irradiation. *J. Hazard. Mater.* **2021**, *407*, 124798. [CrossRef] [PubMed]
42. Liu, Y.-S.; Yamaguchi, A.; Yang, Y.; El Aisnada, A.N.; Uchida, S.; Abe, H.; Ueda, S.; Yamaguchi, K.; Tanabe, T.; Miyauchi, M. Synthesis and Characterization of the Orthorhombic Sn$_3$O$_4$ Polymorph. *Angew. Chem. Int. Ed.* **2023**, *62*, e202300640. [CrossRef]
43. Zhong, D.; Liu, W.; Tan, P.; Zhu, A.; Liu, Y.; Xiong, X.; Pan, J. Insights into the synergy effect of anisotropic {001} and {230} facets of BaTiO$_3$ nanocubes sensitized with CdSe quantum dots for photocatalytic water reduction. *Appl. Catal. B Environ.* **2018**, *227*, 1–12. [CrossRef]
44. Zhu, Y.; Cui, Y.; Xiao, B.; Ou-yang, J.; Li, H.; Chen, Z. Z-scheme 2D/2D g-C$_3$N$_4$/Sn$_3$O$_4$ heterojunction for enhanced visible-light photocatalytic H$_2$ evolution and degradation of ciprofloxacin. *Mater. Sci. Semicond. Process.* **2021**, *129*, 105767. [CrossRef]
45. Feng, S.; Chen, T.; Liu, Z.; Shi, J.; Yue, X.; Li, Y. Z-scheme CdS/CQDs/g-C$_3$N$_4$ composites with visible-near-infrared light response for efficient photocatalytic organic pollutant degradation. *Sci. Total Environ.* **2020**, *704*, 135404. [CrossRef] [PubMed]
46. Liu, B.; Lv, M.; Jiang, W.; Gao, B.; Li, Y.; Zhou, S.; Wang, D.; Liu, C.; Che, G. Self-photoreduced Ag 0-doped Ag (i)–organic frameworks with efficient visible-light-driven photocatalytic performance. *CrystEngComm* **2021**, *23*, 7496–7501. [CrossRef]
47. Yang, C.; Feng, S.; Ma, C.; Zhou, Y.; Dai, X.; Ye, Z.; Wang, Y. Bi$_2$Sn$_2$O$_7$/UiO-66-NH$_2$ heterojunction photocatalyst simultaneously adsorbed and photodegraded tetracycline. *J. Environ. Chem. Eng.* **2023**, *11*, 109664. [CrossRef]
48. Fan, G.; Zhou, J.; Ruan, F.; Li, Y.; Tian, H.; Fan, D.; Chen, Q.; Li, N. The Z-scheme photocatalyst S-BiOBr/Bi$_2$Sn$_2$O$_7$ with 3D/0D interfacial structure for the efficient degradation of organic pollutants. *Sep. Purif. Technol.* **2023**, *309*, 123099. [CrossRef]
49. Heidari, S.; Haghighi, M.; Shabani, M. Ultrasound assisted dispersion of Bi$_2$Sn$_2$O$_7$-C$_3$N$_4$ nanophotocatalyst over various amount of zeolite Y for enhanced solar-light photocatalytic degradation of tetracycline in aqueous solution. *Ultrason. Sonochem.* **2018**, *43*, 61–72. [CrossRef]
50. Huang, S.; Zhang, J.; Qin, Y.; Song, F.; Du, C.; Su, Y. Direct Z-scheme SnO$_2$/Bi$_2$Sn$_2$O$_7$ photocatalyst for antibiotics removal: Insight on the enhanced photocatalytic performance and promoted charge separation mechanism. *J. Photochem. Photobiol. A Chem.* **2021**, *404*, 112947. [CrossRef]
51. Heidari, S.; Haghighi, M.; Shabani, M. Sono-photodeposition of Ag over sono-fabricated mesoporous Bi$_2$Sn$_2$O$_7$-two dimensional carbon nitride: Type-II plasmonic nano-heterojunction with simulated sunlight-driven elimination of drug. *Chem. Eng. J.* **2020**, *389*, 123418. [CrossRef]
52. Wu, S.; Yu, X.; Zhang, J.; Zhang, Y.; Zhu, Y.; Zhu, M. Construction of BiOCl/CuBi$_2$O$_4$ S-scheme heterojunction with oxygen vacancy for enhanced photocatalytic diclofenac degradation and nitric oxide removal. *Chem. Eng. J.* **2021**, *411*, 128555. [CrossRef]
53. Zhang, Y.; Sun, A.; Xiong, M.; Macharia, D.K.; Liu, J.; Chen, Z.; Li, M.; Zhang, L. TiO$_2$/BiOI pn junction-decorated carbon fibers as weavable photocatalyst with UV–vis photoresponsive for efficiently degrading various pollutants. *Chem. Eng. J.* **2021**, *415*, 129019. [CrossRef]
54. Habibi-Yangjeh, A.; Asadzadeh-Khaneghah, S.; Ghosh, S. Anchoring Bi$_4$O$_5$I$_2$ and AgI nanoparticles over g-C$_3$N$_4$ nanosheets: Impressive visible-light-induced photocatalysts in elimination of hazardous contaminates by a cascade mechanism. *Adv. Powder Technol.* **2020**, *31*, 2618–2628. [CrossRef]
55. Shafiq, I.; Hussain, M.; Shehzad, N.; Maafa, I.M.; Akhter, P.; Shafique, S.; Razzaq, A.; Yang, W.; Tahir, M.; Russo, N. The effect of crystal facets and induced porosity on the performance of monoclinic BiVO$_4$ for the enhanced visible-light driven photocatalytic abatement of methylene blue. *J. Environ. Chem. Eng.* **2019**, *7*, 103265. [CrossRef]
56. Feng, Z.; Zeng, L.; Zhang, Q.; Ge, S.; Zhao, X.; Lin, H.; He, Y. In situ preparation of g-C$_3$N$_4$/Bi$_4$O$_5$I$_2$ complex and its elevated photoactivity in Methyl Orange degradation under visible light. *J. Environ. Sci.* **2020**, *87*, 149–162. [CrossRef]